Optics Express, Volume 23, Issue 5, 2015, pp. 6304-6312
DOI:https://doi.org/10.1364/OE.23.006304

High energy transmission annular beam X-ray diffraction

Anthony Dicken,[1] Alex Shevchuk,[1] Keith Rogers,[2] Simon Godber[1] and Paul Evans,[1,*]

[1]*Imaging Science Group, Rosalind Franklin Building, Nottingham Trent University, Nottingham, UK*
[2]*Cranfield Forensic Institute, Cranfield University, Shrivenham, Swindon, UK*
[*]*paul.evans@ntu.ac.uk*

Abstract: We demonstrate material phase retrieval by linearly translating extended polycrystalline samples along the symmetry axis of an annular beam of high-energy X-rays. A series of pseudo-monochromatic diffraction images are recorded from the dark region encompassed by the beam. We measure Bragg maxima from different annular gauge volumes in the form of bright spots in the X-ray diffraction intensity. We present the experiment data from three materials with different crystallographic structural properties i.e. near ideal, large grain size and preferred orientation. This technique shows great promise for analytical inspection tasks requiring highly penetrating radiation such as security screening, medicine and non-destructive testing.

OCIS codes: (050.1940) Diffraction; (340.0340) X-ray optics; (120.5820) Scattering measurements; (340.7440) X-ray imaging.

References and links

1. K. Rogers, P. Evans, J. Rogers, J. Chan, and A. Dicken, "Focal construct geometry – a novel approach to the acquisition of diffraction data," J. Appl. Cryst. **43**(2), 264–268 (2010).
2. G. Harding, H. Fleckenstein, D. Kosciesza, S. Olesinski, H. Strecker, T. Theedt, and G. Zienert, "X-ray diffraction imaging with the multiple inverse fan beam topology: principles, performance and potential for security screening," Appl. Radiat. Isot. **70**(7), 1228–1237 (2012).
3. B. Sun, M. Li, F. Zhang, Y. Zhong, N. Kang, W. Lu, and J. Liu, "The performance of a fast testing system for illicit materials detection based on energy-dispersive X-ray diffraction technique," Microchem. J. **95**(2), 293–297 (2010).
4. C. Crespy, P. Duvauchelle, V. Kaftandjian, F. Soulez, and P. Ponard, "Energy dispersive X-ray diffraction to identify explosive substances: spectra analysis procedure optimization," Nucl. Instrum. Meth. A **623**(3), 1050–1060 (2010).
5. G. Harding, "X-ray scatter tomography for explosives detection," Radiat. Phys. Chem. **71**(3–4), 869–881 (2004).
6. K. Wells and D. A. Bradley, "A review of X-ray explosives detection techniques for checked baggage," Appl. Radiat. Isot. **70**(8), 1729–1746 (2012).
7. I. D. Jupp, P. T. Durrant, D. Ramsden, T. Carter, G. Dermody, I. B. Pleasants, and D. Burrows, "The non-invasive inspection of baggage using coherent X-ray scattering," in *Proceedings of IEEE Conference on Transactions on Nuclear Science* (IEEE, 2000), pp. 1987–1994.
8. S. Pani, E. J. Cook, J. A. Horrocks, J. L. Jones, and R. D. Speller, "Characterization of breast tissue using energy-dispersive X-ray diffraction computed tomography," Appl. Radiat. Isot. **68**(10), 1980–1987 (2010).
9. C. Liu, X. Hua, and W. Zhongchun, "The X-ray diffraction enhanced imaging of lung cancer tissue," in *Proceedings of IEEE 4th International Congress on Image and Signal Processing* (IEEE, 2011), pp. 1593–1595.
10. O. Lazzari, S. Jacques, T. Sochi, and P. Barnes, "Reconstructive colour X-ray diffraction imaging - a novel TEDDI imaging method," Analyst (Lond.) **134**(9), 1802–1807 (2009).
11. A. Dicken, K. Rogers, P. Evans, J. W. Chan, J. Rogers, and S. Godber, "Combined X-ray diffraction and kinetic depth effect imaging," Opt. Express **19**(7), 6406–6413 (2011).
12. S. R. Beath and I. A. Cunningham, "Pseudomonoenergetic X-ray diffraction measurements using balanced filters for coherent-scatter computed tomography," Med. Phys. **36**(5), 1839–1847 (2009).
13. D. O'Flynn, C. B. Reid, C. Christodoulou, M. D. Wilson, M. C. Veale, P. Seller, D. Hills, H. Desai, B. Wong, and R. Speller, "Explosive detection using pixellated X-ray diffraction (PixD)," J. Instrum. **8**(3), P03007 (2013).
14. C. Christodoulou, C. B. Reid, D. O'Flynn, M. Wilson, M. Veale, R. J. Cernik, P. Seller, and R. D. Speller, "Multivariate analysis of pixelated diffraction data," J. Instrum. **6**(12), C12027 (2011).
15. P. Evans, K. Rogers, A. Dicken, S. Godber, and D. Prokopiou, "X-ray diffraction tomography employing an annular beam," Opt. Express **22**(10), 11930–11944 (2014).

#225714 - $15.00 USD Received 27 Oct 2014; revised 22 Jan 2015; accepted 19 Feb 2015; published 2 Mar 2015

16. E. Cook, R. Fong, J. Horrocks, D. Wilkinson, and R. Speller, "Energy dispersive X-ray diffraction as a means to identify illicit materials: a preliminary optimisation study," Appl. Radiat. Isot. **65**(8), 959–967 (2007).
17. G. Harding and A. Harding, "X-ray diffraction imaging for explosives detection," in *Counterterrorist Detection Techniques of Explosives*, J. Yinon, ed. (Elsevier, 2007), pp. 199–235.
18. P. Evans, K. Rogers, J. Chan, J. Rogers, and A. Dicken, "High intensity X-ray diffraction in transmission mode employing an analog of Poisson's spot," Appl. Phys. Lett. **97**(20), 204101 (2010).
19. D. Prokopiou, K. Rogers, P. Evans, S. Godber, J. Shackel, and A. Dicken, "X-ray diffraction with novel geometry," Nucl. Instrum. Meth. A **735**(21), 341–348 (2014).
20. D. Prokopiou, K. Rogers, P. Evans, S. Godber, and A. Dicken, "Discrimination of liquids by a focal construct X-ray diffraction geometry," Appl. Radiat. Isot. **77**, 160–165 (2013).
21. P. Kirkpatrick, "On the theory and use of Ross filters," Rev. Sci. Instrum. **10**(6), 186–191 (1939).
22. P. Kirkpatrick, "Theory and use of Ross filters II," Rev. Sci. Instrum. **15**(9), 223–229 (1944).

1. Introduction

X-ray diffraction (XRD) is a high fidelity laboratory based technique routinely employed for the measurement and characterisation of crystallographic structures in semi and or polycrystalline materials [1,2]. It has been shown to be a suitable tool for a variety of applications including; the identification of illicit materials, controlled substances and explosives [2–7], detection of cancerous tissue [8,9] and non-destructive mapping of the interior of bulk objects [10].

There are two principal X-ray diffraction modalities, namely angular-dispersive X-ray diffraction (ADXRD) and energy-dispersive X-ray diffraction (EDXRD). In ADXRD a sample is illuminated by a tightly collimated beam of monochromatic radiation. The interaction of the incident X-rays with crystalline samples produces diffracted rays when Bragg's condition is satisfied. The angle, 2θ, subtended by the trajectory of the diffracted photons, with respect to the primary beam, is measured to enable the calculation of lattice or d-spacings in a crystalline material. In contrast, EDXRD employs a polychromatic beam to collect diffracted flux from the sample at a fixed 2θ angle. The diffracted photons are incident upon an energy resolving detector, which then enables their wavelength and the sample's d-spacings to be computed. While ADXRD is considered to be the "gold standard" for material specificity [11] it is associated with relatively long data acquisition times as the probability of producing diffracted photons is limited by the monochromised beam. Also, a small beam footprint is required to ensure that the angular resolution and thus d-spacing resolution is not degraded. However, a small gauge volume might contain too few crystals that have the correct orientation to contribute to Bragg scatter [12]. In EDXRD a polychromatic beam increases the probability of producing diffracted flux from the sample. To maintain d-spacing resolution high aspect ratio collimation is required to reduce the acceptance angle for the collected photons. Consequently, a relatively low amount of the total available diffracted flux is measured. A notable exception is the Pixelated X-ray diffraction (PixD) system [13,14], which employs a pencil beam but without diffracted beam collimation. The material specificity of an EDXRD system is also limited by the energy resolving capability of the detector [13–16]. In reality many applications would benefit from a high energy diffraction probe, operating in transmission, with greater penetrating capability for *in situ* measurement. In the case of security screening, Harding et al [17] suggests the use of X-ray energies an order of magnitude greater than those employed by a typical powder diffractometer i.e. ≈8 keV for a Cu target Kα.

In this paper we report material phase retrieval by linearly translating extended polycrystalline samples along the symmetry axis of an annular beam of high-energy X-rays. We employ focal construct geometry (FCG) to produce caustics in the diffracted X-ray distribution and measure their intensity and position using a flat normally positioned detector. An explanation of caustics and our previous low energy FCG work is given in Section 2.1. The relative increase in the diffracted flux offered by FCG is especially important with increasing X-ray energy due to the decreasing coherent scattering cross section. This aspect of FCG enables us to employ a relatively small commercially available tungsten X-ray generator

#225714 - $15.00 USD Received 27 Oct 2014; revised 22 Jan 2015; accepted 19 Feb 2015; published 2 Mar 2015

with a mean spectral energy of ≈58 keV in our experiments. We also demonstrate the first high energy FCT movie sequences and associated diffractograms collected from three different polycrystalline samples.

This work for the first time extends the FCG approach to high energies and unlike previous technology we record high energy X-ray caustics to enable greater penetrating capability for *in situ* measurement. Also, the axial translation of the sample along the beam enables a rigid source/detector configuration, which is a promising basis for a relatively compact high energy instrument.

The paper is organised as follows. Section 2 presents the theory background, our new high energy technique and describes the experiment conditions. Section 3 presents our experiment results and discussion. Section 4 summarizes our conclusions, discusses the broader implications of our findings and the future direction of the work.

2. Methods

2.1 Theory background

The detailed theory of focal construct geometry (FCG) and annular beam scanning employing low X-ray energies (i.e. ≈17 keV) has been described in detail elsewhere [1,15,18]. To recap, FCG is an alternate powder diffraction technique that employs an annular interrogating beam of radiation rather than a conventional pencil or line beam. It has been shown to increase the intensity of the diffracted flux recorded at the detector by ≈20 times. It has also been shown to mitigate against structural complexities such as preferred orientation and large grain size [18,19], as well as being employed to differentiate between threat and non-threat liquid samples [20] in a security context. We have also demonstrated X-ray diffraction tomography by raster scanning a sample through an annular beam of X-rays [15].

The principle of operation of FCG is that a continuum of Debye cones originates from within an annular gauge volume at characteristic angles according to Bragg's condition. These overlapping Debye cones form bright circular or spot patterns referred to as caustics upon a detection plane, normal to the annular beam symmetry axis. We have previously defined caustics in geometric terms, as the envelope of a family of curves, formed by overlapping Debye rings incident upon a plane [15]. The shape of the caustic is a curve, which is tangent to each member of a family of Debye rings at some point [15]. In addition, we adopt the term "focal spot" to describe on-axis caustics as distinct from secondary or off-axis caustics.

In this paper we employed balanced filtering [21,22] to produce pseudo-monochromatic diffraction images. Detailed theory regarding balanced filtering is described elsewhere [12,21,22].

2.2 New high energy technique

Our high energy approach employs the axial translation of an extended sample along a high energy annular X-ray beam to create focal spots on a detector. These bright spots are a function of the diffraction angle 2θ of a corresponding family of Debye cones, providing that $2\theta > \varphi$, as shown in Fig. 1.

#225714 - $15.00 USD Received 27 Oct 2014; revised 22 Jan 2015; accepted 19 Feb 2015; published 2 Mar 2015

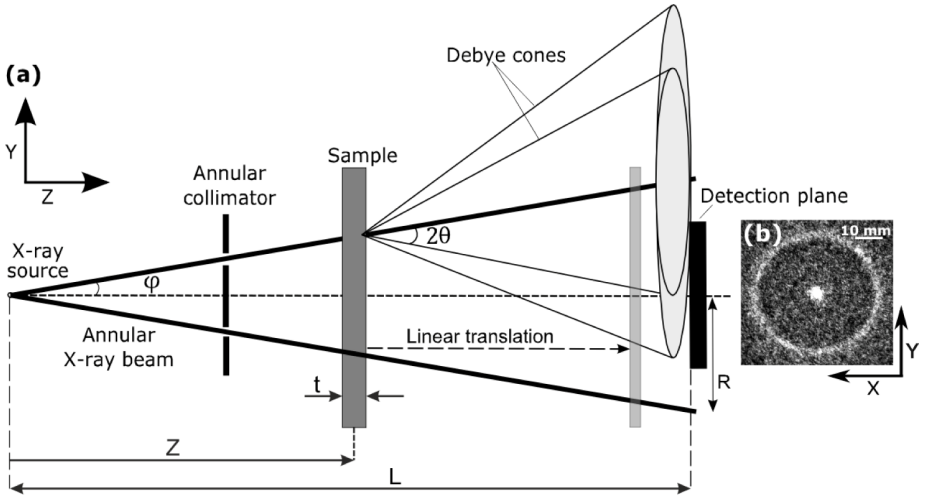

Fig. 1. Schematic depicting the full optical path of the FCG experiment arrangement. (a) The position of a Debye cone of half-opening angle 2θ originating at an annular gauge volume at position Z. (b) Example of a detector image of a high intensity circular caustic and focal spot produced by diffracted flux from a $CaCO_3$ sample.

In this scheme each focal spot is collected from a different annular gauge volume at a known source to sample distance Z during the scan. Providing that the annular beam parameters; half-opening angle φ, radius R at the detector plane and source to detector distance L are known then the diffraction angle 2θ is given by

$$2\theta = \varphi + \tan^{-1}\left(\left(\frac{R}{L-Z}\right) - \tan\varphi\right). \tag{1}$$

The corresponding d-spacing may be derived by substituting for θ in Bragg's condition $\lambda = 2d\sin\theta$ to give

$$d = \frac{\lambda}{2\sin\left[\frac{1}{2}\left(\varphi + \tan^{-1}\left(\left(\frac{R}{L-Z}\right) - \tan\varphi\right)\right)\right]}. \tag{2}$$

The geometric unsharpness ΔZ resulting from sample thickness, t, measured along the Z-axis, the divergence of the annular beam and the effective spectral width of the X-rays is given by

$$\Delta Z = Z_{Max} - Z_{Min} \tag{3}$$

where the sample positions along the Z-axis, Z_{Max} and $-Z_{Min}$, are given by

$$Z_{Max} = L\left(1 - \frac{\tan\varphi_{Min}}{\tan(2\theta_{Max} - \varphi_{Min}) + \tan\varphi_{Min}}\right) + \frac{t}{2} \tag{4}$$

$$Z_{Min} = L\left(1 - \frac{\tan\varphi_{Max}}{\tan(2\theta_{Min} - \varphi_{Max}) + \tan\varphi_{Max}}\right) - \frac{t}{2}. \tag{5}$$

Where φ_{Max} and φ_{Min} are the half-opening angles subtended by the outer and inner boundaries of the annular beam with respect to the symmetry axis, respectively. The divergence is assumed to be symmetrical i.e. $\varphi = \varphi_{Max} + \varphi_{Min}/2$. The diffraction

#225714 - $15.00 USD Received 27 Oct 2014; revised 22 Jan 2015; accepted 19 Feb 2015; published 2 Mar 2015

angles, $2\theta_{Max}$ and $2\theta_{Min}$, correspond to the d-spacing under consideration at the maximum and minimum wavelengths, respectively i.e. the range of the effective spectral content of the annular beam.

2.3 Experiment conditions

X-rays were generated by a Hamamatsu microfocus X-ray source (model L9181-02) with a tungsten target (W Kα ≈59.3 keV) and a focal spot size of 40 μm; the accelerating voltage and current were 130 kV, 300 μA, respectively. Rare earth metal filters thulium (Tm; K-edge 59.39 keV) and erbium (Er; K-edge 57.49 keV) were selected with a thicknesses of 0.1 mm to create an energy passband of 1.9 keV about the tungsten Kα lines [7]. An annular beam was produced using a bespoke tungsten optic with $\varphi = 3.87^\circ \pm 0.05^\circ$ opening angle (i.e. $\varphi_{Max} = 3.92^\circ, \varphi_{Min} = 3.82^\circ$). The annular beam symmetry axis was oriented normal to the detector plane using a 5 axis Thorlab motion stage (x,y,z, pitch and yaw) with < 1.5 μm bidirectional repeatability and minimum repeatable increment movement of 0.2 μm. The scattered X-ray photons were collected by a stationary 4 inch Hamamatsu X-ray image intensifier incorporating an 0.5 mm aluminium window and caesium iodide phosphor with terbium doped gadolinium oxysulphide (Gd2O2S:Tb) phosphor screen, which was optically coupled to a 1280x1024 (6.45 μm) 12 bit cooled Bigeye G-132B low noise CCD camera. The intensifier input window was positioned downstream of the X-ray source (i.e. 899 mm from X-ray source) within the circular opaque shadow cast by the annular optic. The 0.1 mm Tm and Er filters were used in sequence, with the sample placed in a bespoke sample holder and scanned along the Z-axis between the collimator and the detector, see Fig. 1, with each frame being integrated for 10 seconds. The resulting image is the difference between the two filtered images (Tm-Er) and records X-rays with a mean energy of 58.4 keV [12]. Traditional format 1D diffractograms were produced by integrating the signal obtained from a 0.7 mm^2 area at the centre of the intensifier input window for each sample position and converted into d-spacing using Eq. (2). These diffractograms were smoothed using a Savitzky Golay filter (via MATLAB® (R2012b)). Reference patterns for each sample were collected on a PANalytical X'Pert PRO diffractometer operating at ≈8 keV (Cu Kα). Comparisons between the FCG and traditional patterns are presented in Section 3.

2.4 Materials

Three materials with significantly different crystallographic properties were selected for analysis:

1) 10 mm thick $CaCO_3$ powder held in a powder-cell (i.e. a near X-ray transparent container) that exhibited randomly oriented crystals resulting in complete Debye cones and thus diffraction caustics with a high degree of rotational symmetry;

2) 0.5 mm thick sheet of copper that exhibited preferred orientation as a result of its manufacturing process;

3) 10 mm thick NaCl (held in a powder-cell) that exhibited relatively large grain size.

Samples were placed at 141 mm on the Z axis and translated along this axis by 551 mm (from the X-ray source). A stepwise translation employed a constant 0.5 mm step, providing a maximum angular resolution of 0.003° and a minimum of 0.04°, with corresponding upper and lower d-spacing resolution at the W Kα line of 0.0018 Å and 0.0017 Å, respectively.

3. Results and Discussion

Two-dimensional FCG diffraction images are illustrated in Figs. 2-4 for the three different samples at various distances along the Z axis. Figure 2 illustrates diffraction images transmitted through 10 mm of $CaCO_3$ powder, a near-ideal polycrystalline sample, which was

#225714 - $15.00 USD Received 27 Oct 2014; revised 22 Jan 2015; accepted 19 Feb 2015; published 2 Mar 2015

expected to create geometrically complete Debye cones with uniform intensity Debye rings. Although the circular intensity distributions illustrated in Fig. 2 resemble Debye rings they are, in reality, caustics formed by the summation of Debye rings from the annular gauge volumes. Altering the sample to detector distance enables the caustics to be "focused" at the detector and enable the pre-focus, see [Fig. 2(c)], focal spot, see [Fig. 2(b)] and post focus, see [Fig. 2(a)] conditions to be studied. Interrogating the pixels collected from a central region of approximately 0.7 mm^2 on the detector (i.e. about the piercing point of the annular beam symmetry axis) for each sample position during the scan enables the production of a 1D diffractogram similar to those one might obtain from a traditional diffractometer. Figure 5 illustrates good agreement between the 1D diffraction pattern for $CaCO_3$ obtained by high energy FCG and that from a Cu target diffractometer described previously in Section 2.3. Figure 3 illustrates the diffraction images obtained from a 0.5 mm thick copper sample. Preferred orientation effects (introduced from rolling during manufacture) results in distorted diffraction caustics for Bragg maxima in a pre-focus, see [Fig. 3(a)] or post-focus, see [Fig. 3(c)] sample to detector position. However high intensity focal spots are generated, see [Fig. 3(b)] at the centre of the detector. The peak positions in the 1D diffractogram are unaffected and good agreement can be seen, see Fig. 6, between the FCG pattern and a standard diffractogram. Discontinuous caustics are recorded for samples with preferred orientation and for samples with large grain size, see Fig. 3 and Fig. 4, respectively. A powerful feature of the FCG technique is that the focal spots from discontinuous diffracted flux still occur at the correct angular position to conserve the integrity of the 1D diffractogram, see Fig. 7.

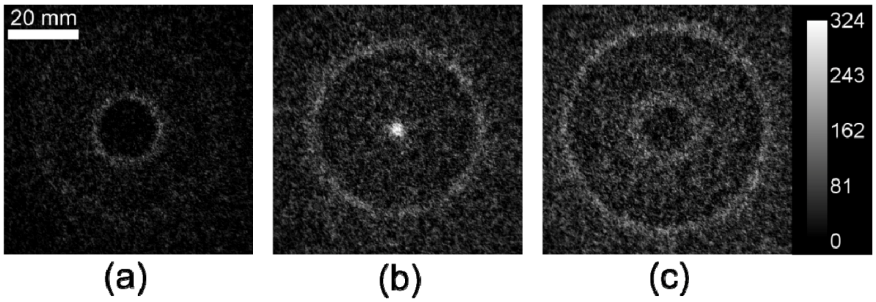

Fig. 2. Experiment images collected by FCG from a $CaCO_3$ sample showing the diffraction caustics before (a), at (b), and after (c), a focal spot. The corresponding Z-axis sample positions were 141 mm, 358.5 mm and 421.5 mm, respectively. The three images were taken from a video sequence of the caustics from the sample during its axial translation (Media 1). The focal spot (b) was obtained for inter-planar spacing d = 1.89 Å, 2θ = 6.44°.

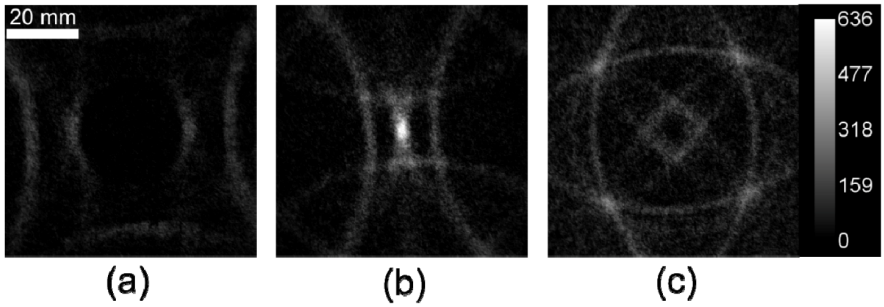

Fig. 3. Experiment images collected by FCG from a copper sample showing the diffraction caustics before (a), at (b), and after (c), a focal spot. The corresponding Z-axis positions were 141 mm, 301 mm and 575.5 mm, respectively. The three images were taken from a video sequence of the caustics from the sample during its axial translation (Media 2). The focal spot (b) was obtained for inter-planar spacing d = 2.09 Å, 2θ = 5.82 °.

#225714 - $15.00 USD Received 27 Oct 2014; revised 22 Jan 2015; accepted 19 Feb 2015; published 2 Mar 2015

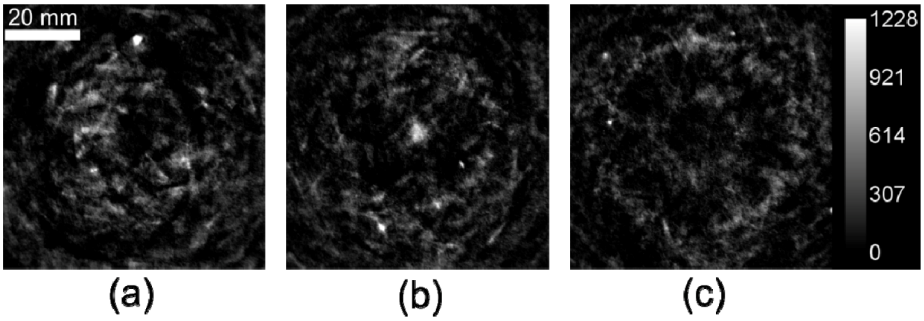

Fig. 4. Experiment images collected by FCG from a NaCl sample showing the diffraction caustics before (a), at (b), and after (c), a focal spot. The corresponding Z-axis positions were 257 mm, 329.5 mm and 409.5 mm, respectively. The three images were taken from a video sequence of the caustics from the sample during its axial translation (Media 3). The focal spot (b) was obtained for inter-planar spacing d = 1.99 Å, 2θ = 6.11 °.

Experimentally we have observed that balanced filtering significantly improved the signal to noise ratio (SNR) in comparison with a single filter e.g. it increases the SNR from ≈2:1 (Tm only) to 11:1 (Tm–Er) when applied to the $CaCO_3$ sample. In all cases the 1D diffractograms obtained by FCG exhibit slightly wider peaks than those collected with a standard diffractometer. The calculation of the geometric unsharpness ΔZ .using Eqs. (3)-(5) enabled a good estimate of the peak widths for all the relatively strong diffraction peaks, as highlighted in the diffractograms shown in Figs. 5, Fig. 6 and Fig. 7, which incorporate horizontal bars to indicate calculated peak widths centred on the corresponding d-spacings. The peak widths recorded for the relatively thin copper sample, t = 0.5 mm, are of the same order of magnitude as those recorded for the 10 mm thick NaCl sample and the 10 mm thick $CaC0_3$ sample, as predicted by Eqs. (3)-(5). This observation confirms that the beam divergence and the effective spectral width were significant contributors to peak broadening.

These considerations outline the inherent penalty of conducting diffraction experiments in transmission mode. However, given the significantly larger gauge volume employed by FCG i.e. mm penetration as opposed micron penetration with traditional diffractometers operating at Cu Kα wavelengths the increase in Bragg maxima width was expected. It should be noted that this comparison cannot be explored experimentally on a traditional diffractometer (in transmission mode) because thicker, mm scale, samples render meaningful measurements impractical due to the near complete attenuation of the diffracted X-rays in transmission.

In consideration of the FCT optical design it can be appreciated from equation Eqs. (3)-(5) that increasing φ can reduce the geometric unsharpness and potentially lower the d-spacing error as well as reducing the source/detector separation L. However, it is required that $2\theta > \varphi$ to effect a focal spot condition. In practice, this renders 2θ values that marginally exceed φ as impractical due to excessively large standoff distances. Consequently, FCT design requires careful evaluation of φ to accommodate the material(s) to be measured. For example, metals often require relatively small d-spacing analysis (i.e. large φ) in comparison to drugs or polymers, which require large d-spacing measurement (i.e. small φ).

#225714 - $15.00 USD Received 27 Oct 2014; revised 22 Jan 2015; accepted 19 Feb 2015; published 2 Mar 2015

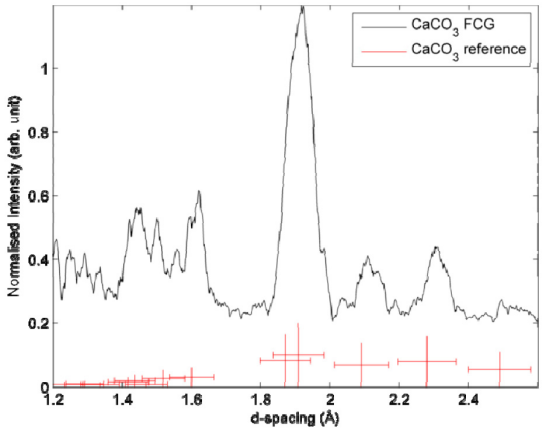

Fig. 5. Comparison of the 1D diffractogram obtained from high energy FCG for a $CaCO_3$ sample with a reference pattern of the same material measured on a standard diffractometer.

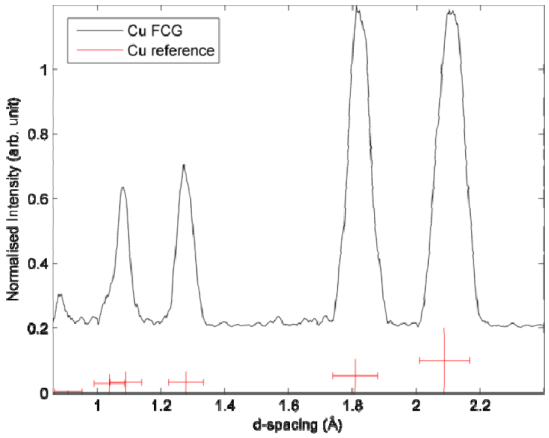

Fig. 6. Comparison of the 1D diffractogram obtained from high energy FCG for a copper sample with a reference pattern of the same material measured on a standard diffractometer.

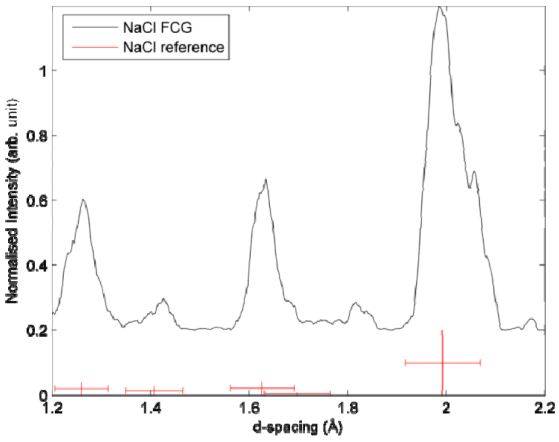

Fig. 7. Comparison of the 1D diffractogram obtained from high energy FCG for a NaCl sample with a reference pattern of the same material measured on a standard diffractometer.

#225714 - $15.00 USD Received 27 Oct 2014; revised 22 Jan 2015; accepted 19 Feb 2015; published 2 Mar 2015

4. Conclusion

We have demonstrated for the first time that a high energy annular X-ray beam can be employed to record focal spots in the diffracted flux intensity from an axially translated sample. This result is promising as the ratio of coherent scattering cross section for W Kα (≈58 keV) wavelengths to Cu Kα (≈8 keV) wavelengths is approximately 1:17 for the materials presented here. The detection of the high energy focal spots enabled the calculation of the associated 2θ diffraction angles and d-spacings for material phase identification. Also, because 2θ diffraction angles decrease with increasing X-ray beam energy then a typical diffraction pattern (1-4Å) is spread over around 1/8 of the angular range at W Kα wavelengths in comparison with Cu Kα wavelengths. However, FCG copes favourably with the angular measurement of relatively long throw focal spots because $\delta\theta/\delta Z$ reduces with increasing sample to detector distance i.e. decreasing values of Z from simple optical leaver considerations. We also show that high energy focal spots are formed from discontinuous Debye rings produced by complex crystallographic structures exhibiting preferred orientation or large grain size.

It is hoped that this work will serve as the basis for time critical *in situ* materials discrimination measurements of relatively thick materials, cm scale, which requires the increased penetration capability of high energy X-rays. Further efforts will concentrate on testing high energy FCG with spatially complex samples and using the dynamic caustic images to analyse other crystallographic properties of samples. We believe that there are many potential applications for a high energy X-ray material specific probe in security screening, medicine and non-destructive testing.

Acknowledgments

This programme of work is funded by the EPSRC grant number EP/K020196/1 and also the Innovative Research Call in Explosives and Weapons Detection Initiative. The latter is a cross-government programme under the UK government's CONTEST strategy, sponsored by a number of departments and agencies, in partnership with the US Department of Homeland Security.

#225714 - $15.00 USD Received 27 Oct 2014; revised 22 Jan 2015; accepted 19 Feb 2015; published 2 Mar 2015